Journal of Energy Chemistry 109 (2025) 177–185

Contents lists available at ScienceDirect

Journal of Energy Chemistry

journal homepage: www.elsevier.com/locate/jechem

http://www.journals.elsevier.com/journal-of-energy-chemistry/

Enhanced hole extraction through in situ mixed self-assembled molecules for efficient inverted perovskite solar cells

Xiang He [a,b], Qi Wang [b], Shantao Zhang [a], Yajuan Li [b,c], Xuefei Weng [b], Irfan Ismail [b], Chang-Qi Ma [b,*], Shangfeng Yang [a,*], Yi Cui [b,*]

[a] *Key Laboratory of Precision and Intelligent Chemistry, Collaborative Innovation Center of Chemistry for Energy Materials (iChEM), Department of Materials Science and Engineering, University of Science and Technology of China, Hefei 230026, Anhui, China*

[b] *i-lab, Vacuum Interconnected Nanotech Workstation, Suzhou Institute of Nano-Tech and NanoBionics, Chinese Academy of Sciences, Suzhou 215123, Jiangsu, China*

[c] *Key Laboratory of Intelligent Optoelectronic Devices and Chips of Jiangsu Higher Education Institutions, Advanced Technology Research Institute of Taihu Photon Center, School of Physical Science and Technology, Suzhou University of Science and Technology, Suzhou 215009, Jiangsu, China*

ARTICLE INFO

Article history:
Received 8 April 2025
Revised 30 April 2025
Accepted 14 May 2025
Available online 22 May 2025

Keywords:
Mixed self-assembled monolayers
Energy level alignment
Interface engineering
Vacancy filling
Wide-bandgap
Inverted perovskite solar cells

ABSTRACT

Self-assembled monolayers (SAMs), owing to their amphiphilic nature, tend to aggregate, which impedes the formation of a dense and uniform SAM on the substrate. Additionally, the weak adsorption ability of SAMs on the indium tin oxide (ITO) surface and the desorption of hydroxyl (OH) from the ITO surface induced by polar solvents can lead to the formation of vacancies. Herein, a dimethylacridine-based SAM is incorporated into the perovskite precursor solution. This SAM can be extruded from the precursor solution and enriched on the bottom surface of the perovskite, filling the vacancies and in situ forming a mixed SAM with MeO-2PACz as a hole-selective layer (HSL). The in situ formed mixed SAM optimizes the energy level alignment between the HSL and the perovskite, facilitating hole extraction and alleviating the residual strain of the perovskite film. Consequently, the perovskite solar cells (PSCs), based on the mixed SAM, achieve a power conversion efficiency (PCE) of 25.69% and exhibit excellent operational stability. When this approach is applied to 1.78 eV bandgap PSC devices, it yields a PCE of 20.08%. This work presents a unique strategy for fabricating both high-quality perovskite films and superior buried interfaces, which is also applicable to wide-bandgap PSCs.

1. Introduction

Organic-inorganic mixed halide perovskite solar cells (PSCs) have become prominent competitors in the photovoltaic field, attributed to their exceptional optoelectronic performance and low cost, such as high-power conversion efficiency (PCE), adjustable optical bandgap, high carrier mobility, and low-temperature solution preparation [1–6]. Recently, the certified champion PCE of inverted PSCs has reached 26.95% for single-junction devices [7], highlighting their vast potential for integration into energy systems. Despite these advancements, interface energy loss caused by non-radiative recombination in perovskite films prevents PSCs from achieving the Shockley-Queisser (S-Q) limit of PCE and hinders its commercial application, especially the bottom interface of perovskite films, which has been rarely studied [8–11]. Recent studies have shown that high-performance inverted PSCs can be fabricated using self-assembled monolayers (SAMs) as hole-selective layers (HSLs), such as [2-(3,6-dimethoxy-9H-carbazol-9-yl)ethyl]phosphonic acid (MeO-2PACz), [2-(9H-carbazol-9-yl)ethyl]phosphonic acid (2PACz), and [4-(3,6-dimethyl-9H-carbazol-9-yl)butyl]phosphonic acid (Me-4PACz) [12–15]. Such a SAM HSL can be prepared by directly spin-coating SAM solution onto the substrate. Alternatively, He et al. reported a process of doping dimethylacridine molecules into perovskite precursors, which effectively passivated the grain boundaries of perovskite and achieved a certified PCE of 25.39% [16]. However, utilizing a single SAM for high-quality passivation of perovskite bottom interfaces is quite challenging. For example, Me-4PACz and MeO-2PACz tend to aggregate due to their amphiphilicity, impeding the formation of a uniform, dense, and wettable SAM film on the substrate [17–19].

---

* Corresponding authors.

E-mail addresses: cqma2011@sinano.ac.cn (C.-Q. Ma), sfyang@ustc.edu.cn (S. Yang), ycui2015@sinano.ac.cn (Y. Cui).

https://doi.org/10.1016/j.jechem.2025.05.025
2095-4956/

These factors will also affect the crystallization of perovskite and the quality of thin films.

SAM with high density, strong wettability, and few defects is crucial for the fabrication of high-performance inverted PSCs [18,20]. To this end, mixing another organic molecule with SAM to form a so-called mixed SAM layer can not only improve the SAM coverage but also reduce the recombination of charge carriers at the interface and enhance hole extraction capability [21–23]. The mixed SAM strategy can also promote perovskite growth and regulate surface energy levels, which is important for improving device efficiency and stability. For instance, Magomedov et al. reported that adding 6dPA to the Me-4PACz precursor solution significantly improved the wettability of the Me-4PACz hole selective monolayer, leading to a substantial enhancement in device performance [24]. Yan et al. demonstrated that depositing a layer of 1,3-bis(diphenylphosphino)propane (DPPP) on the SAM strengthened the bonding between the HSL and perovskite bottom interface, resulting in a significant improvement in device performance [25]. Fang et al. used 2PACz as the initial HSL, followed by modification with Me-4PACz. This interface engineering, which changed the potential distribution of 2PACz on the indium tin oxide (ITO) surface and buried a denser perovskite film at the interface, improved the energy level alignment between the perovskite and the HSL, effectively suppressing non-radiative recombination. Ultimately, the fill factor (FF) and open-circuit voltage (V_{OC}) of the device were significantly improved [17].

Herein, we develop a new approach to fabricate mixed SAM through an in situ strategy, by employing MeO-2PACz as a HSL and incorporating [4-(2,7-dibromo-9,9-dimethylacridin-10(9H)-yl)butyl]phosphonic acid (DMAcPA) into the perovskite precursor, which can be extruded from the precursor solution and enriched at the bottom of the perovskite during the quenching crystallization process with chlorobenzene, thus in situ forming mixed SAM combined with MeO-2PACz. The in situ formed mixed SAM strategy combines the advantages of traditional mixed SAM and double-layer SAM, fills adsorption vacancies, improves the energy level alignment between the perovskite and the HSL, suppresses non-radiative recombination, and enhances hole extraction. Morever, it passivates perovskite grain boundaries, leading to an overall improvement of the perovskite film. As a result, compared with the control device bearing single MeO-2PACz SAM, the target device based on the mixed SAM exhibits a significant increase in PCE from 23.32% to 25.69%. Additionally, we applied this strategy to a 1.78 eV wide bandgap (WBG) PSC, which can increase the PCE from 18.16% to 20.08%, demonstrating the universality of this in situ-formed mixed SAM approach.

2. Results and discussion

Two SAM molecules, DMAcPA and MeO-2PACz, were selected, with their molecular structures shown in Fig. 1(a). Density functional theory (DFT) calculations reveal that the molecular dipole moment of DMAcPA (μ = 3.5 D) is greatly higher than that of MeO-2PACz (μ = 0.2 D; Fig. 1a), which is beneficial for hole transport [26]. DFT also calculated the highest occupied molecular orbital/lowest unoccupied molecular orbital (HOMO/LUMO) orbitals and energy levels of both SAMs (Fig. S1). Initially, MeO-2PACz molecules were deposited on ITO, and the SAM monolayer was formed through chemical adsorption between the –OH groups on the ITO surface and the acidic anchoring groups [27]. However, the weak adsorption ability of MeO-2PACz on the ITO surface can lead to the formation of vacancies. During the antisolvent chlorobenzene extraction process, many dimethyl sulfoxide (DMSO)-PbI_2 molecules inevitably appear at the bottom interface, and annealing can lead to the formation of vacancies at this interface [17]. To address this issue, DMAcPA molecules were added to the perovskite precursor solution. During the quenching crystallization process of chlorobenzene, the DMAcPA molecules are extruded from the precursor solution to the bottom surface of the perovskite film, thus in situ forming mixed SAM combined with MeO-2PACz to serve as HSL, as illustrated in Fig. 1(b). Therefore, the vacancies were filled; meanwhile, DMAcPA molecules can interact with the perovskite to some extent (Fig. S2), promoting the crystallization of perovskite.

Based on the in situ mixed SAM strategy, inverted devices with structure ITO/MeO-2PACz/$Cs_{0.05}(FA_{0.95}MA_{0.05})_{0.95}Pb(I_{0.95}Br_{0.05})_3$/Passivation layer/PCBM/BCP/Ag were fabricated (PCBM: [6,6]-phenyl C61 butyric acid methyl ester, BCP: 2,9-dimethyl-4,7-diphenyl-1,10-phenanthroline). The current density-voltage (*J-V*) curves of the champion devices are illustrated in Fig. 2(a), the maximum PCE of the control device is 23.32%, with a V_{OC} of 1.138 V, a short-circuit current density (J_{SC}) of 25.16 mA cm^{-2}, and an FF of 81.51%. A series of optimization processes were carried out (Figs. S3–S8, Tables S1–S6), and the maximum PCE of the target device is achieved as 25.69% with a V_{OC} of 1.179 V, a J_{SC} of 25.50 mA cm^{-2}, and an FF of 85.49%, while the optimal device based on double-layer SAM is only 24.31% (Fig. S6 and Table S4). In addition to the obvious PCE increase, the hysteresis in the target device is notably reduced compared to the control device (Fig. 2b), the corresponding photovoltaic parameters are summarized in Table 1. The integrated current value measured by external quantum efficiency (EQE) testing is consistent with the J_{SC} value obtained from *J-V* measurement, as shown in Fig. 2(c).

The bandgap of the perovskite thin film was determined to be 1.56 eV via ultraviolet-visible absorption spectroscopy (Fig. S9). The incorporation of DMAcPA molecules did not alter the bandgap of the perovskite. Additionally, the target device achieved a stabilized power output (SPO) of 25.51% at its maximum power point (MPP) (V_{max} = 1.04 V) after 500 s of continuous 1-sun illumination (Fig. 2d).

To evaluate the reproducibility of in situ mixed SAM strategy, 40 devices were independently fabricated in a single batch. The statistical photovoltaic parameters are presented in Fig. 2(e), demonstrating the improved reproducibility of the target devices. The analysis of the statistical photovoltaic parameters reveals that the enhanced PCE of the target device is primarily attributed to the enhancements in V_{OC} and FF (Fig. S10). Meanwhile, due to the favorable energy level alignment, hole extraction is facilitated, which in turn contributes to the improvement of the FF.

In addition, this strategy was applied to 1.78 eV wide bandgap (WBG) PSCs (Fig. 2f). The target device achieved a V_{OC} of 1.33 V, rather higher than that of the control device (1.26 V), the FF increased from 81.42% to 84.38%, the J_{SC} increased from 17.73 to 17.89 mA cm^{-2}, and the PCE of the device has also increased from 18.16% to 20.08%. This is one of the higher V_{OC} values reported by WBG (1.75–1.79 eV) PSCs (Table S7). The EQE for the champion target device in Fig. 2(f) shows an integrated J_{SC} of 17.66 mA cm^{-2}, which approaches the value 17.89 mA cm^{-2} obtained from the *J-V* curves. We also conducted statistical analysis on 40 devices to verify the universality of the in situ mixed SAM strategy in WBG PSCs (Fig. S11). After 300 s of continuous 1-sun illumination, the target WBG device showed better stability (Fig. S12).

The crystallinity and morphology of perovskite films were characterized using scanning electron microscopy (SEM). As shown in Fig. 3(a), the target perovskite film exhibits enlarged grain size from 297 to 360 nm (see insets) and reduced grain boundaries, indicating better crystal quality, consistent with the X-ray diffraction (XRD) results (Fig. S13 and Table S8), while excess PbI_2 (circle marking on the top surface, Fig. S14) and a small number of holes have been observed in the control perovskite film (circle marking on the bottom surface, Fig. 3a). Peel-off method of the bottom

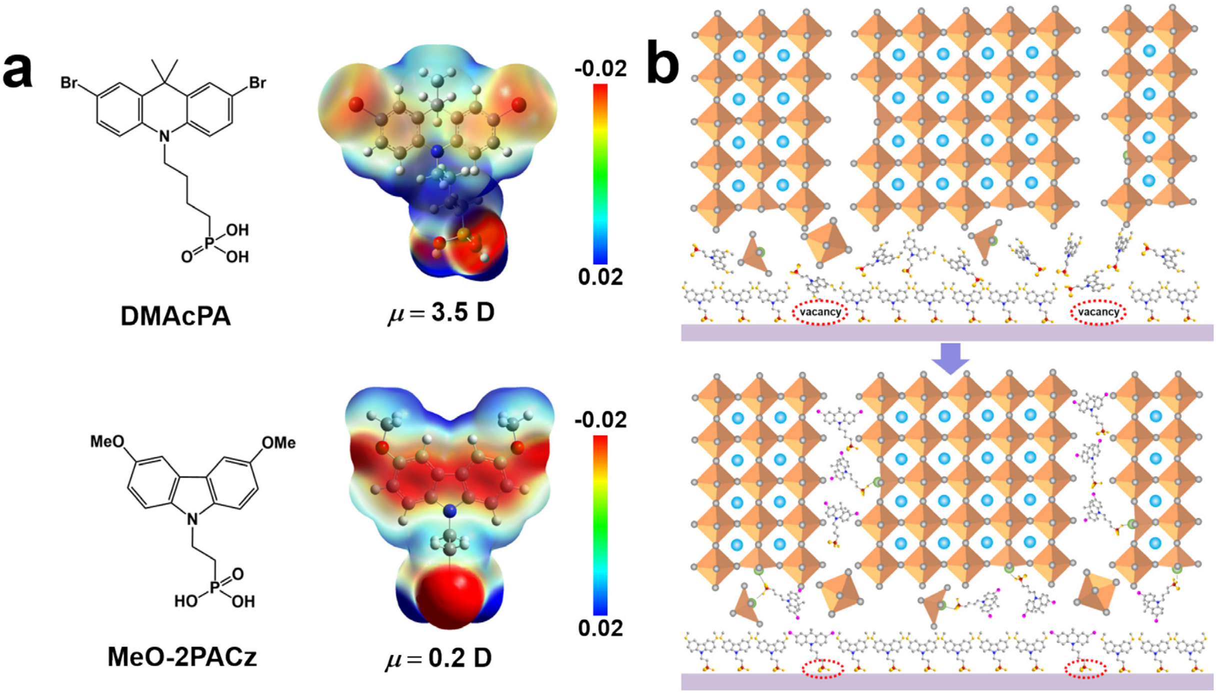

Fig. 1. (a) Molecular structures, calculated molecular dipole moments, and electrostatic surface potential maps. (b) Schematic diagram of molecule deposition. By extruding DMAcPA molecules to the bottom interface of perovskite, the vacancies are filled, promoting the formation of crystalline and dense perovskite layers.

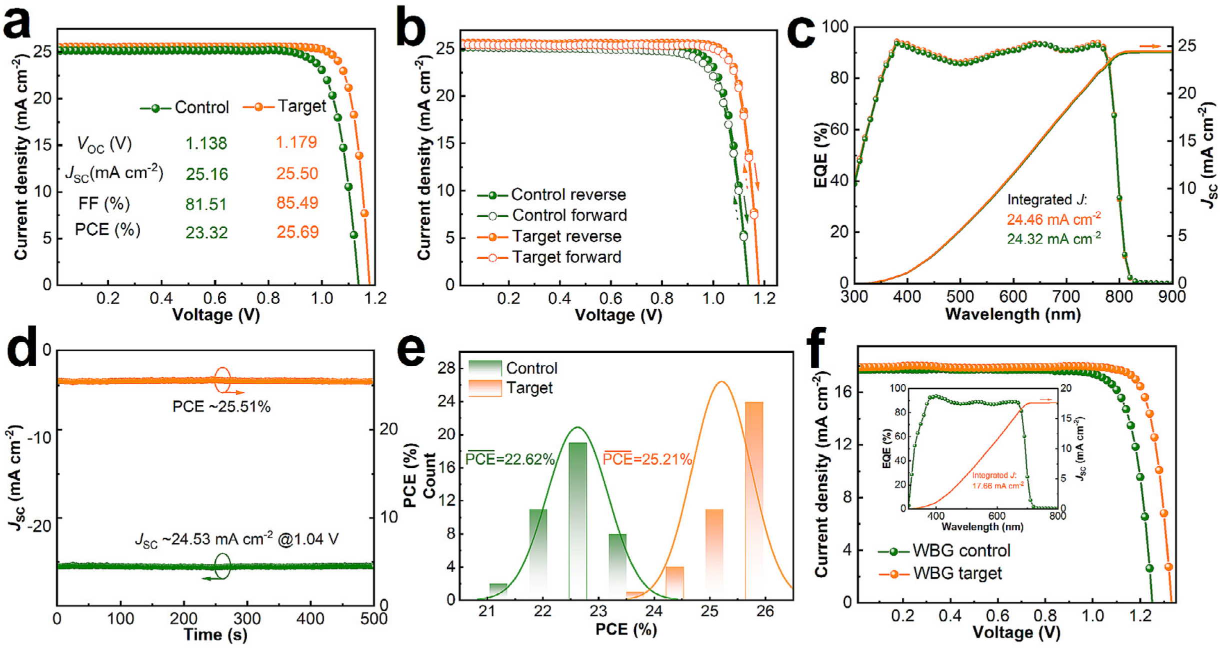

Fig. 2. (a) *J-V* curves and (b) champion device from reverse and forward scan. (c) EQE spectra and the corresponding integrated current of the control and target device. (d) The SPO at the MPP for the target champion device. (e) Histogram of the PCE. (f) *J-V* curves of WBG PSCs. The insertion diagram is the EQE of the target device.

Table 1

Photovoltaic parameters of the control and target champion devices.

		V_{OC} (V)	J_{SC} (mA cm^{-2})	FF (%)	PCE (%)	Hysteresis index (%) [a]
Control	Reserve	1.138	25.16	81.51	23.32	3.3
	Forward	1.137	25.23	78.64	22.55	
Target	Reserve	1.179	25.50	85.49	25.69	1.1
	Forward	1.179	25.43	84.76	25.41	

[a] Hysteresis index (HI) = [PCE (Reverse)–PCE (Forward)]/PCE (Reverse).

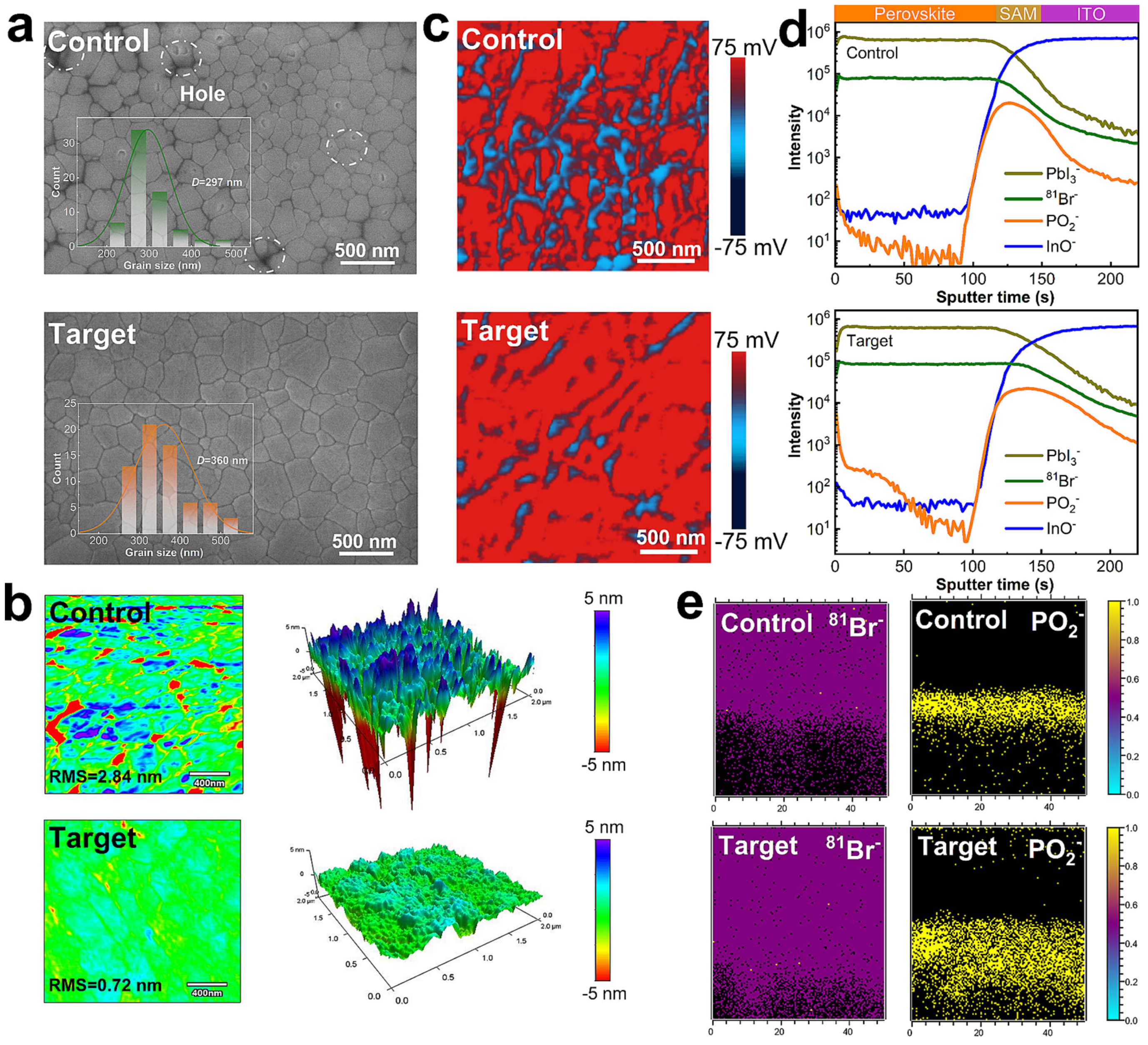

Fig. 3. (a) The SEM images of perovskite bottom surfaces. Inset: the corresponding histograms of grain size distributions of the perovskite films. The dotted white circles mark the pinholes. (b) AFM images of perovskite bottom interface. (c) AFM-IR images of the bottom interface of perovskite films. (d) TOF-SIMS depth profiles of perovskite films and (e) negative ions two-dimensional-mapping of the samples.

interface of perovskite film is shown in the Fig. S15. Through atomic force microscopy (AFM), the roughness of the perovskite film is verified, as shown in Fig. 3(b) and Fig. S16, and both the top and bottom surfaces of the target perovskite film show lower roughness compared to the control. To further investigate the distribution of the SAM at the bottom of perovskite, atomic force microscopy-based infrared spectroscopy (AFM-IR) was employed (Fig. 3c). We observed a more uniform distribution of P–C bonds at the bottom of the target film through the P–C vibration peak at 1400 cm^{-1} [16], which is consistent with the formation of a uniformly dense SAM layer.

Additionally, time-of-flight secondary ions mass spectroscopy (TOF-SIMS) measurements reveal that DMAcPA molecules are enriched at the bottom of the perovskite [16], as evidenced by the appearance of enhanced $^{81}Br^{-}$ and PO_2^{-} signals in the target films, with a correspondingly stronger signal. This finding indicates, to some extent, the enrichment of SAM molecules at the perovskite bottom interface (Fig. 3d and e). This suggests that the vacancies caused by the aggregation of MeO-2PACz molecules are filled and the density of SAM molecules increases, which corresponds to the results in Fig. 3(c) and Fig. S17. Therefore, the hole transport ability and electron blocking ability are increased.

X-ray photoelectron spectroscopy (XPS) measurements were conducted to investigate the potential impact of buried interface interactions on the crystallization of perovskite thin films (Fig. S18). The I 3*d* and Pb 4*f* peaks of the target perovskite film exhibit an apparent shift compared to the control. In addition, in the O 1*s* spectra, the peak positions corresponding to the P=O group (530.9 eV) and the P–OH group (531.8 eV) of the target film are shifted as well. The shift of O 1*s* and Pb 4*f* peaks indicates the formation of covalent bonds (P=O–Pb) between phosphonates and Pb. Meanwhile, in the O 1*s* spectrum, the peak of 530.2 eV represents metal–oxygen, which also confirms this viewpoint. Additionally, the shift of the P–OH group peak indicates the formation of hydrogen bonds, which is attributed to the high electronegativity of oxygen [17]. These findings provide additional evidence that the mixed SAM leads to better perovskite thin films, thereby contributing to improving device performance.

The arrangement of the underlying SAM also impacts the energy levels. The work function (WF) at the bottom and top interfaces of perovskite was measured using ultraviolet photoelectron spectroscopy (UPS) (Fig. 4a and b). The top interface WF of the control and target perovskite film is −4.65 and −4.54 eV, and the bottom interface WF is −4.39 and −4.84 eV. In addition, the WF of the

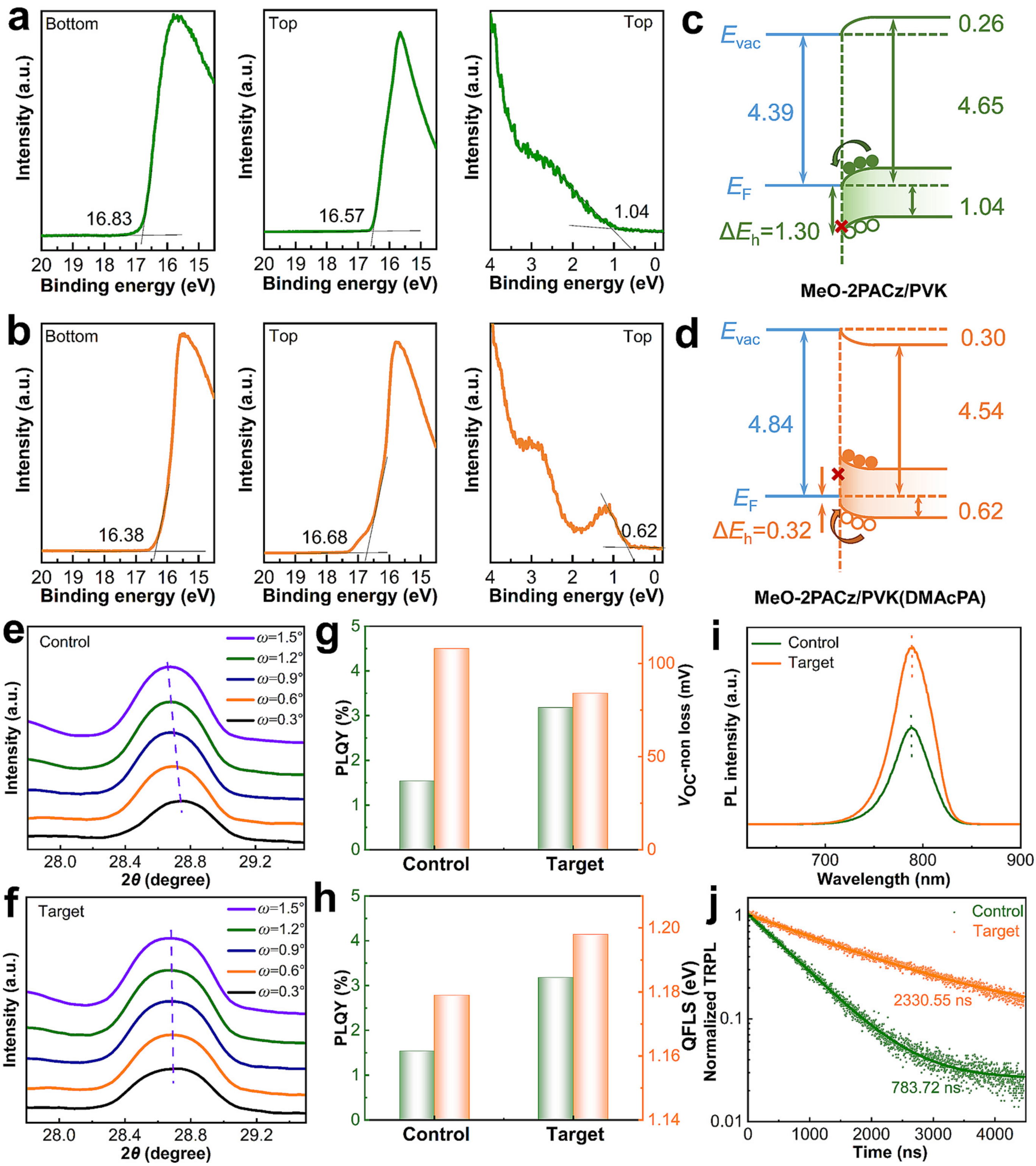

Fig. 4. UPS and energy-level diagrams for the (a, c) control and (b, d) the target perovskite films. GIWAXS patterns of (e) control and (f) target perovskite film. (g) PLQY and the corresponding V_{OC} non-radiative recombination loss. (h) The PLQY and corresponding QFLS. (i) PL and (j) TRPL spectra of perovskite films, all the samples were deposited on the bare glass.

top and bottom interfaces based on the MeO-2PACz/DMAcPA/Perovskite structure is −4.40 and −4.62 eV, respectively. According to the band arrangement principle of Schottky contacts, in the case of MeO-2PACz/perovskite (Fig. 4c), the band of the perovskite bends downward, thereby creating a potential barrier for hole extraction. This configuration facilitates the transfer of electrons to ITO, ultimately resulting in a device PCE of only 23.32%. For MeO-2PACz/perovskite (DMAcPA) (Fig. 4d), owing to its more pronounced p-type character and a deeper Fermi level, the perovskite band bends upward and the offset (ΔE_h) is as low as 0.32 eV, improving the hole extraction rate at the interface [16]. However, for MeO-2PACz/DMAcPA/perovskite (Fig. S19), although the perovskite band is bent upwards, which can promote hole extraction and block electrons, the ΔE_h is relatively high at 0.60 eV.

The internal stress of the perovskite films was investigated by grazing incidence wide-angle X-ray scattering (GIWAXS) [28]. The graphs in Fig. 4(e and f) are transformed and fitted through Fig. S20, and the transformation formula is

$$q = \frac{4\pi \sin\theta}{\lambda}$$

where λ is the wavelength of the incident X-ray and θ is half of the incidence angle. As the incident angle increased from 0.3° to 1.5°, the 2θ = 28.7° peak of the control perovskite film gradually shifted towards a smaller angle, which may be due to the formation of voids [17]. In contrast, the peak of the target film shows a minimal change, and the corresponding fitting line slope of the lattice distance spacing (D-spacing) is lower (Fig. S21), suggesting a reduction in residual strain. As large residual strain in the perovskite layers was commonly caused by excessive lattice shrinkage [29], these results indicate that mixed SAM effectively alleviates the residual strain of perovskite film. Therefore, increasing the density of SAM molecules, improving energy level arrangement, and releasing stress help enhance carrier transport and reduce recombination, ultimately improving device performance.

The photoluminescence quantum yield (PLQY) is used to evaluate the degree of non-radiative recombination in perovskite films. We spin-coated perovskite thin films on ITO substrates and measured their corresponding PLQY (Fig. 4g). Obviously, the target perovskite films showed a higher PLQY (3.18%) than the control one (1.54%). A higher PLQY indicates a decrease in non-radiative recombination and an increase in radiative recombination. The V_{OC} losses caused by non-radiative recombination are also greatly decreased (from 108 to 84 mV) [8,17]. Furthermore, internal electron-hole quasi-Fermi level splitting (QFLS) was calculated based on PLQY values (Fig. 4h) [30,31]. The control displays a QFLS of 1.179 V, which increases to 1.198 V for the target perovskite. The mixed SAM optimizes the energy level alignment and ameliorates the internal defects of the perovskite film, thus enhancing the V_{OC} of the device. Additionally, steady-state photoluminescence (PL) and time-resolved photoluminescence spectroscopy (TRPL) were used to investigate the carrier recombination behavior in perovskite films [32–34]. As shown in Fig. 4(i), the target perovskite film exhibits higher PL peak intensity. Furthermore, the carrier lifetime (τ_{ave}) of target perovskite film, obtained by fitting the TRPL curve, dramatically increases from 738.72 to 2330.55 ns (Fig. 4j and Table S9). The prolonged carrier lifetime along with enhanced PL intensity suggests effective suppression of non-radiative recombination.

We also characterized the carrier dynamics and defect passivation characteristics of the device. The relationship between V_{OC} and logarithmic light intensity can be plotted using the following formula [35–38].

$$V_{OC} = \frac{nK_BT}{q}\ln P_{light} + A$$

where q is the elementary charge, K_B is Boltzmann's constant, T is the temperature, n is the ideal factor, and A is constant. As shown in Fig. 5(a), the fitted n values were 1.48 and 1.17 for the control and target device, respectively. The n value of the target device is closer to 1, indicating less trap-assisted recombination.

Next, FF will be analyzed to investigate how optimizing charge extraction affects the FF of the device (Fig. 5b). Firstly, the impact

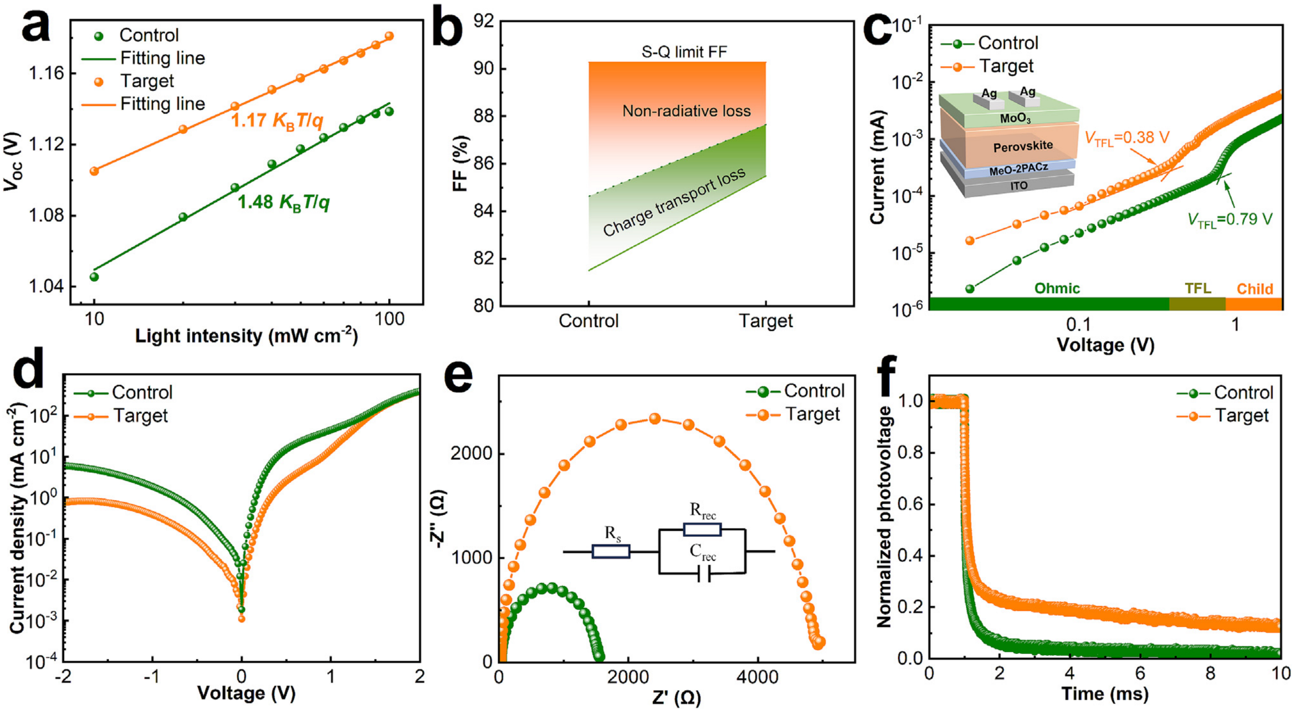

Fig. 5. (a) Seminatural logarithmic plots of V_{OC} versus light intensity. (b) FF loss analysis, analyzing the impact of non-radiative loss and charge transfer loss. (c) I-V and (d) dark J_D-V curves of the hole-only devices. (e) Nyquist plot of the device. (f) TPV measurement of devices.

of non-radiative losses and charge transport losses was analyzed. The maximum FF (FF_{max}) that neglects charge transport loss is calculated according to the equation [39].

$$FF_{max} = \frac{\nu_{OC} - \ln(\nu_{OC} + 0.72)}{\nu_{OC} + 1}$$

$$\nu_{OC} = \frac{V_{OC}}{nK_B T/q}$$

Therefore, the FF_{max} values for the target and control perovskite devices are 87.65% and 84.63%, respectively. The S-Q theoretical limit of perovskite solar cell devices with a bandgap width of 1.556 eV is 90.28%. The actual measured FF for the target and control perovskite devices is 85.49% and 81.51%, respectively. The actual measured FF, FF_{max}, and S-Q theoretical limits are caused by charge transfer loss and non-radiative loss, respectively, which demonstrates that the optimized charge transport is the main reason for the enhancement of FF. Therefore, optimized charge transport is also one of the reasons for the FF enhancement.

In order to analyze the trap-state density (N_{trap}) in the PSCs, the space-charge limited current (SCLC) measurements were conducted on the hole-only devices with a structure of ITO/MeO-2PACz/perovskite layer/MoO_3/Ag. The N_{trap} is calculated via the formula [40–42].

$$N_{trap} = \frac{2\varepsilon_r\varepsilon_0 V_{TFL}}{qL^2}$$

As depicted in Fig. 5(c), the trap-filled limit voltage (V_{TFL}) of the control and target devices is 0.79 and 0.38 V, respectively. The responding N_{trap} is 6.28×10^{15} and 3.02×10^{15} cm^{-3}, respectively. These results indicate that there are fewer defects in the target device and trap-assisted recombination is suppressed. The hole mobility (μ_h) of devices was also obtained using the Mott-Gurney square law given by the following equation [43,44].

$$J = \frac{9\varepsilon_r\varepsilon_0\mu V^2}{8L^3}$$

where J is the current density, ε_0 is the vacuum permittivity, and ε_r is the relative permittivity of the perovskite medium. Fig. S22 displays the $J^{1/2}$-V curves of the hole-only devices. The μ_h value of the target devices increased from 1.14×10^{-2} to 2.58×10^{-2} cm^2 V^{-1} s^{-1}. The substantial enhancement in μ_h suggested that a high hole transport efficiency was achieved in the target devices. Besides, as shown in the dark current J_D-V curves of the PSCs (Fig. 5d), the target device exhibits significantly reduced leakage current [45], more efficient hole transfer, and excellent diode characteristics under the voltage regions of ±2–0 V.

The electrical characteristics of the devices were characterized using electrochemical impedance spectroscopy (EIS) (Fig. 5e). The

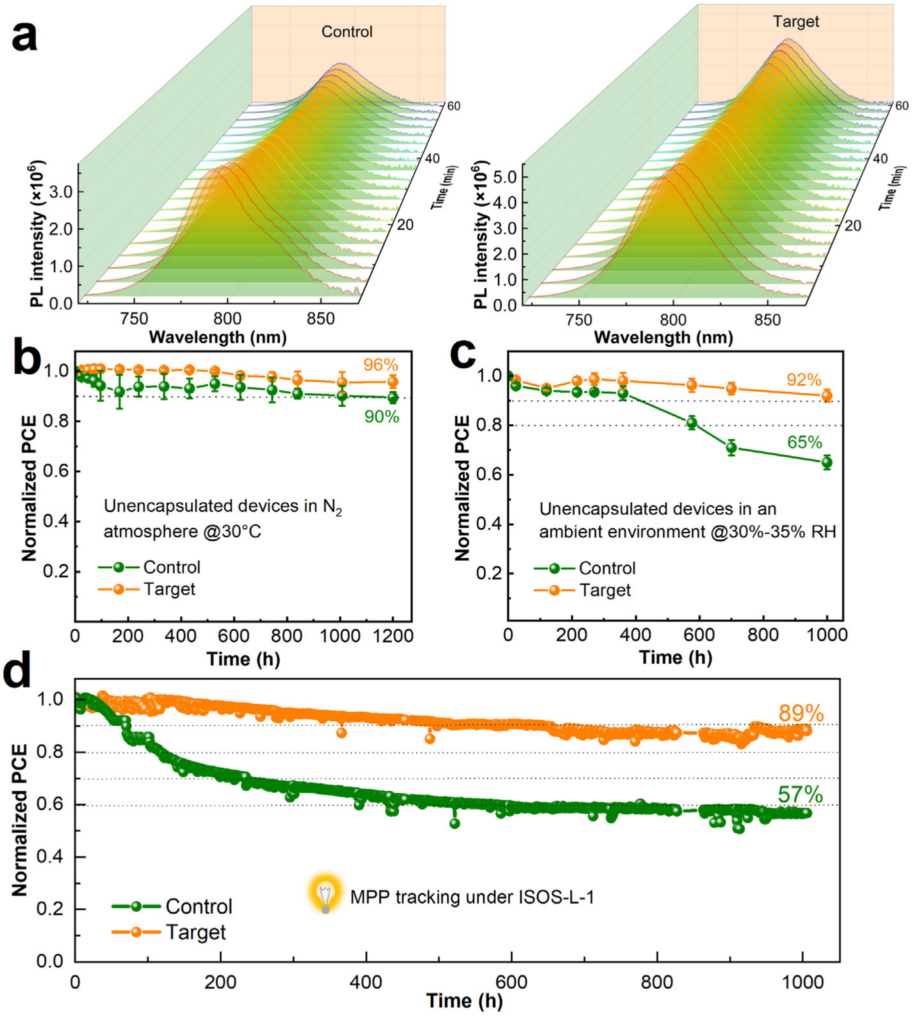

Fig. 6. (a) Time-dependent PL spectra of perovskite films in ambient air with RH 50%–60% for 60 min, and test every 3 min. Storage stability test of unpackaged devices (b) in inert atmosphere, (c) under RH 30%–35% stability, and (d) operational stability of devices under MPP tracking with continuous illumination at 30 ± 5 °C.

recombination resistance (R_{rec}) of the control device is calculated to be 1551 Ω, while the R_{rec} of the target device is increased to 4961 Ω. Moreover, the series resistance (R_s) also shows a decreasing trend, from 30.1 Ω in control to 28.5 Ω in target. The decreased series resistance and markedly increased recombination resistance contributed to the suppressed charge recombination and increased carrier collection. As a result, the significantly improved V_{OC} and FF can be achieved in the target device. The carrier transport in the device was further investigated through transient photovoltage (TPV) decay measurement [46]. As shown in Fig. 5(f), the TPV results show that the lifetime of the target device is extended, which is in good agreement with the suppression of non-radiative recombination at high V_{OC}.

The PL spectra of perovskite films tested continuously for 60 min in the air with relative humidity (RH) of 50%–60% showed that the target film maintained 79% of its initial intensity, while the control only maintained 48% (Fig. 6a). As shown in Fig. 6(b), the unencapsulated target device maintains 96% of the initial PCE after 1200 h of storage in nitrogen at room temperature, while the control device remains only 90%. The humidity stability of unencapsulated devices was tracked under ambient conditions (temperature: ~30 °C, RH: 30%–35%), as illustrated in Fig. 6(c). The target device maintained its initial efficiency of 92%, significantly exceeding the 65% of the control device under the same conditions. Furthermore, the effect of mixed SAM on the moderate operational stability of the PSC device is also evaluated by tracking the unencapsulated devices at MPP tracking with the ISOS-L-1 protocol. As shown in Fig. 6(d), the target device maintains 89% of the initial efficiency after 1000 h of continuous illumination, whereas the control device only retains 57% under the same conditions. The improvement of the operational and light stabilities of the target device is attributed to the enhanced crystallinity of the perovskite film, the reduced trap density, and the improved quality of the SAM layer.

3. Conclusions

To summarize, we propose a novel in situ mixed SAM strategy for efficient inverted PSCs. We added dimethylacridine-based SAM molecules to the perovskite precursor, which can be extruded from the precursor solution and enriched at the bottom of the perovskite film to form a mixed SAM combined with MeO-2PACz during the quenching crystallization process of chlorobenzene. On the one hand, it can enhance the energy level alignment between the HSL and the perovskite, facilitating hole extraction and suppressing non-radiative recombination at the interface. On the other hand, it also alleviates the stress of the perovskite film, achieving improved crystallinity of the perovskite film. As a result, the target device achieved a PCE of 25.69%. Moreover, when this strategy was applied to WBG PSCs, it led to an increase in PCE from 18.16% to 20.08%. This research offers a unique perspective for fabricating both high-quality perovskite bulk films and superior buried interfaces.

Experimental section

Experimental details can be found in the Supporting Information.

CRediT authorship contribution statement

Xiang He: Writing – original draft, Methodology, Investigation, Formal analysis, Conceptualization. **Qi Wang:** Writing – review & editing, Visualization, Resources. **Shantao Zhang:** Writing – review & editing, Visualization, Formal analysis. **Yajuan Li:** Writing – review & editing, Visualization, Formal analysis. **Xuefei Weng:** Writing – review & editing, Visualization, Formal analysis. **Irfan Ismail:** Visualization, Formal analysis. **Chang-Qi Ma:** Writing – review & editing, Visualization, Formal analysis. **Shangfeng Yang:** Writing – review & editing, Validation, Resources, Funding acquisition, Data curation. **Yi Cui:** Writing – review & editing, Resources, Project administration, Funding acquisition, Data curation.

Declaration of competing interest

The authors declare that they have no known competing financial interests or personal relationships that could have appeared to influence the work reported in this paper.

Acknowledgments

This work was supported by the Young Cross Team Project of CAS (No. JCTD-2021-14), the National Natural Science Foundation of China (51925206) and Gusu Innovation and Entrepreneur Leading Talents (ZXL2022466). We thank Qing Zhang, Zhongmiao Gong, Rong Huang, Zhiyun Li, Xiaotian Ge, and Leilei Xu from NANO-X for the GIWAXS, AFM, TOF-SIMS, XPS, PL, and SEM measurements. We thank Prof. Yusheng Wang from Soochow University for the EQE measurement.

Appendix A. Supplementary material

Supplementary data to this article can be found online at https://doi.org/10.1016/j.jechem.2025.05.025.

References

[1] H. Chen, C. Liu, J. Xu, A. Maxwell, W. Zhou, Y. Yang, Q. Zhou, A.S.R. Bati, H. Wan, Z. Wang, L. Zeng, J. Wang, P. Serles, Y. Liu, S. Teale, Y. Liu, M.I. Saidaminov, M. Li, N. Rolston, S. Hoogland, T. Filleter, M.G. Kanatzidis, B. Chen, Z. Ning, E.H. Sargent, Science 384 (2024) 189–193. https://doi.org/10.1126/science.adm9474.

[2] X. Chen, Q. Wang, H. Wei, J. Yang, Y. Yao, W. Tang, W. Qiu, X. Xu, L. Song, Y. Wu, Q. Peng, Energy Environ. Sci. 17 (2024) 7342–7354. https://doi.org/10.1039/d4ee02964j.

[3] Q. Jiang, K. Zhu, Nat. Rev. Mater. 9 (2024) 399–419. https://doi.org/10.1038/s41578-024-00678-x.

[4] L. Li, M. Wei, V. Carnevali, H. Zeng, M. Zeng, R. Liu, N. Lempesis, F.T. Eickemeyer, L. Luo, L. Agosta, M. Dankl, S.M. Zakeeruddin, U. Roethlisberger, M. Grätzel, Y. Rong, X. Li, Adv. Mater. 36 (2024) 2303869. https://doi.org/10.1002/adma.202303869.

[5] R. Guo, X. Zhang, X. Zheng, L. Li, M. Li, Y. Zhao, S. Zhang, L. Luo, S. You, W. Li, Z. Gong, R. Huang, Y. Cui, Y. Rong, H. Zeng, X. Li, Adv. Funct. Mater. 33 (2023) 2211955. https://doi.org/10.1002/adfm.202211955.

[6] D. Li, Y. Huang, Z. Ren, A. Amini, A.B. Djurišić, C. Cheng, G. Li, J. Energy Chem. 79 (2023) 168–191. https://doi.org/10.1016/j.jechem.2022.12.029.

[7] Best Research-Cell Efficiency Chart. https://www.nrel.gov/pv/cell-efficiency.html. (accessed on 15 May 2025).

[8] Y. Zheng, Y. Li, R. Zhuang, X. Wu, C. Tian, A. Sun, C. Chen, Y. Guo, Y. Hua, K. Meng, K. Wu, C.-C. Chen, Energy Environ. Sci. 17 (2024) 1153–1162. https://doi.org/10.1039/d3ee03435f.

[9] Z.-W. Gao, Y. Wang, W.C.H. Choy, Adv. Energy Mater. 12 (2022) 2104030. https://doi.org/10.1002/aenm.202104030.

[10] X. Jiang, B. Liu, X. Wu, S. Zhang, D. Zhang, X. Wang, S. Gao, Z. Huang, H. Wang, B. Li, Z. Xiao, T. Chen, A.K.Y. Jen, S. Xiao, S. Yang, Z. Zhu, Adv. Mater. 36 (2024) 2313524. https://doi.org/10.1002/adma.202313524.

[11] Y. Huang, K. Yan, X. Wang, B. Li, B. Niu, M. Yan, Z. Shen, K. Zhou, Y. Fang, X. Yu, H. Chen, L. Zhang, C.Z. Li, Adv. Mater. 36 (2024) 2408101. https://doi.org/10.1002/adma.202408101.

[12] Q. Cao, T. Wang, X. Pu, X. He, M. Xiao, H. Chen, L. Zhuang, Q. Wei, H.-L. Loi, P. Guo, B. Kang, G. Feng, J. Zhuang, G. Feng, X. Li, F. Yan, Adv. Mater. 36 (2024) 2311970. https://doi.org/10.1002/adma.202311970.

[13] X. He, H. Chen, J. Yang, T. Wang, X. Pu, G. Feng, S. Jia, Y. Bai, Z. Zhou, Q. Cao, X. Li, Angew. Chem. Int. Ed. 63 (2024) e202412601. https://doi.org/10.1002/anie.202412601.

[14] X. Jiang, X. Wang, X. Wu, S. Zhang, B. Liu, D. Zhang, B. Li, P. Xiao, F. Xu, H. Lu, T. Chen, A.K.Y. Jen, S. Yang, Z. Zhu, Adv. Energy Mater. 13 (2023) 2300700. https://doi.org/10.1002/aenm.202300700.

[15] R. He, W. Wang, Z. Yi, F. Lang, C. Chen, J. Luo, J. Zhu, J. Thiesbrummel, S. Shah, K. Wei, Y. Luo, C. Wang, H. Lai, H. Huang, J. Zhou, B. Zou, X. Yin, S. Ren, X. Hao, L. Wu, J. Zhang, J. Zhang, M. Stolterfoht, F. Fu, W. Tang, D. Zhao, Nature 618 (2023) 80–86. https://doi.org/10.1038/s41586-023-05992-y.

[16] Q. Tan, Z. Li, G. Luo, X. Zhang, B. Che, G. Chen, H. Gao, D. He, G. Ma, J. Wang, J. Xiu, H. Yi, T. Chen, Z. He, Nature 620 (2023) 545–551. https://doi.org/10.1038/s41586-023-06207-0.

[17] H. Cui, L. Huang, S. Zhou, C. Wang, X. Hu, H. Guan, S. Wang, W. Shao, D. Pu, K. Dong, J. Zhou, P. Jia, W. Wang, C. Tao, W. Ke, G. Fang, Energy Environ. Sci. 16 (2023) 5992–6002. https://doi.org/10.1039/d3ee02818f.

[18] M. Liu, L. Bi, W. Jiang, Z. Zeng, S.-W. Tsang, F.R. Lin, A.-K.-Y. Jen, Adv. Mater. 35 (2023) 2304415. https://doi.org/10.1002/adma.202304415.

[19] J. Wu, P. Yan, D. Yang, H. Guan, S. Yang, X. Cao, X. Liao, P. Ding, H. Sun, Z. Ge, Adv. Mater. 36 (2024) 2401537. https://doi.org/10.1002/adma.202401537.

[20] M. Li, M. Liu, F. Qi, F.R. Lin, A.K.Y. Jen, Chem. Rev. 124 (2024) 2138–2204. https://doi.org/10.1021/acs.chemrev.3c00396.

[21] Z. Dai, S.K. Yadavalli, M. Chen, A. Abbaspourtamijani, Y. Qi, N.P. Padture, Science 372 (2021) 618–622. https://doi.org/10.1126/science.abf5602.

[22] W. Jiang, F. Li, M. Li, F. Qi, F.R. Lin, A.K.-Y. Jen, Angew. Chem., Int. Ed. 61 (2022) e202213560. https://doi.org/10.1002/anie.202213560.

[23] H. Chen, A. Maxwell, C. Li, S. Teale, B. Chen, T. Zhu, E. Ugur, G. Harrison, L. Grater, J. Wang, Z. Wang, L. Zeng, S.M. Park, L. Chen, P. Serles, R.A. Awni, B. Subedi, X. Zheng, C. Xiao, N.J. Podraza, T. Filleter, C. Liu, Y. Yang, J.M. Luther, S. De Wolf, M.G. Kanatzidis, Y. Yan, E.H. Sargent, Nature 613 (2023) 676–681. https://doi.org/10.1038/s41586-022-05541-z.

[24] A. Al-Ashouri, M. Marčinskas, E. Kasparavičius, T. Malinauskas, A. Palmstrom, V. Getautis, S. Albrecht, M.D. McGehee, A. Magomedov, ACS Energy Lett 8 (2023) 898–900. https://doi.org/10.1021/acsenergylett.2c02629.

[25] C. Li, X. Wang, E. Bi, F. Jiang, S.M. Park, Y. Li, L. Chen, Z. Wang, L. Zeng, H. Chen, Y. Liu, C.R. Grice, A. Abudulimu, J. Chung, Y. Xian, T. Zhu, H. Lai, B. Chen, R.J. Ellingson, F. Fu, D.S. Ginger, Z. Song, E.H. Sargent, Y. Yan, Science 379 (2023) 690–694. https://doi.org/10.1126/science.ade3970.

[26] H. Zhang, S. Zhang, X. Ji, J. He, H. Guo, S. Wang, W. Wu, W.-H. Zhu, Y. Wu, Angew. Chem. Int. Ed. 63 (2024) e202401260. https://doi.org/10.1002/anie.202401260.

[27] Y. Zhang, Y. Liu, Z. Zhao, T. Kong, W. Chen, W. Liu, P. Gao, D. Bi, Adv. Funct. Mater. 35 (2024) 2417575. https://doi.org/10.1002/adfm.202417575.

[28] J. Chen, X. Fan, J. Wang, J. Wang, J. Zeng, Z. Zhang, J. Li, W. Song, ACS Nano 18 (2024) 19190–19199. https://doi.org/10.1021/acsnano.4c04768.

[29] X. Wu, G. Xu, F. Yang, W. Chen, H. Yang, Y. Shen, Y. Wu, H. Chen, J. Xi, X. Tang, Q. Cheng, Y. Chen, X.-M. Ou, Y. Li, Y. Li, ACS Energy Lett. 8 (2023) 3750–3759. https://doi.org/10.1021/acsenergylett.3c01167.

[30] X. Jiang, L. Jia, S. Zhang, Y. Gao, N. Yan, T. Hou, S. Gao, X. Wang, X. Li, W. Chen, Z. Xiao, X. Wu, Z. Fang, S. Liu, S. Yang, Angew. Chem. Int. Ed. 63 (2024) e202412409. https://doi.org/10.1002/anie.202412409.

[31] S. Liu, J. Li, W. Xiao, R. Chen, Z. Sun, Y. Zhang, X. Lei, S. Hu, M. Kober-Czerny, J. Wang, F. Ren, Q. Zhou, H. Raza, Y. Gao, Y. Ji, S. Li, H. Li, L. Qiu, W. Huang, Y. Zhao, B. Xu, Z. Liu, H.J. Snaith, N.-G. Park, W. Chen, Nature 632 (2024) 536–542. https://doi.org/10.1038/s41586-024-07723-3.

[32] N. Yan, X. Ren, Z. Fang, X. Jiang, Z. Xu, L. Zhang, S. Ren, L. Jia, J. Zhang, Y. Du, D. Zhao, K. Zhao, S. Yang, S. Liu, Adv. Funct. Mater. 32 (2022) 2201384. https://doi.org/10.1002/adfm.202201384.

[33] X. He, T. Xu, J. Zhang, S. Yang, W. Song, Y. Cui, W. Zhang, ACS Appl. Energy Mater. 7 (2024) 7838–7843. https://doi.org/10.1021/acsaem.4c01430.

[34] R. Liu, X. Zheng, Z. Wang, M. Zeng, C. Lan, S. Yang, S. Li, A. Wang, M. Li, J. Guo, X. Weng, Y. Rong, X. Li, J. Energy Chem. 100 (2025) 646–652. https://doi.org/10.1016/j.jechem.2024.09.007.

[35] X. He, T. Xu, X. Zhang, S. Gong, W. Zhang, W. Song, ACS Appl. Energy Mater. 6 (2023) 981–988. https://doi.org/10.1021/acsaem.2c03425.

[36] X. Li, X. Wu, B. Li, Z. Cen, Y. Shang, W. Lian, R. Cao, L. Jia, Z. Li, D. Gao, X. Jiang, T. Chen, Y. Lu, Z. Zhu, S. Yang, Energy Environ. Sci. 15 (2022) 4813–4822. https://doi.org/10.1039/D2EE02543D.

[37] W. Zhou, L. Jia, M. Chen, X. Li, Z. Su, Y. Shang, X. Jiang, X. Gao, T. Chen, M. Wang, Z. Zhu, Y. Lu, S. Yang, Adv. Funct. Mater. 32 (2022) 2201374. https://doi.org/10.1002/adfm.202201374.

[38] Y. Zheng, X. Yang, R. Su, P. Wu, Q. Gong, R. Zhu, Adv. Funct. Mater. 30 (2020) 2000457. https://doi.org/10.1002/adfm.202000457.

[39] X. Wu, D. Zhang, B. Liu, Y. Wang, X. Wang, Q. Liu, D. Gao, N. Wang, B. Li, L. Wang, Z. Yu, X. Li, S. Xiao, N. Li, M. Stolterfoht, Y.-H. Lin, S. Yang, X.C. Zeng, Z. Zhu, Adv. Mater. 36 (2024) 2410692. https://doi.org/10.1002/adma.202410692.

[40] Y. Li, Y. Duan, Z. Liu, L. Yang, H. Li, Q. Fan, H. Zhou, Y. Sun, M. Wu, X. Ren, N. Yuan, J. Ding, S. Yang, S. Liu, Adv. Mater. 36 (2024) 2310711. https://doi.org/10.1002/adma.202310711.

[41] Y. Qi, M. Almtiri, H. Giri, S. Jha, G. Ma, A.K. Shaik, Q. Zhang, N. Pradhan, X. Gu, N. I. Hammer, D. Patton, C. Scott, Q. Dai, Adv. Energy Mater. 12 (2022) 2202713. https://doi.org/10.1002/aenm.202202713.

[42] X. Yuan, X. Ling, H. Wang, C. Shen, R. Li, Y. Deng, S. Chen, J. Energy Chem. 96 (2024) 249–258. https://doi.org/10.1016/j.jechem.2024.04.036.

[43] J.W. Jung, W.H. Jo, Adv. Funct. Mater. 20 (2010) 2355–2363. https://doi.org/10.1002/adfm.201000164.

[44] F. Fei, Y. Liao, Y. Xu, S. Wang, L. Li, X. Dong, X. Zhou, J. Gao, K. Wang, N. Yuan, J. Ding, ACS Appl. Mater. Interfaces 16 (2024) 24760–24770. https://doi.org/10.1021/acsami.4c02559.

[45] Y. Huang, M. Tao, Y. Zhang, Z. Wang, Z. Sun, W. Zhang, Y. Xiong, X. Zong, Y. Wang, M. Liang, Angew. Chem. Int. Ed. 64 (2024) e202416188. https://doi.org/10.1002/anie.202416188.

[46] Y. Yang, Q. Xiong, J. Wu, Y. Tu, T. Sun, G. Li, X. Liu, X. Wang, Y. Du, C. Deng, L. Tan, Y. Wei, Y. Lin, Y. Huang, M. Huang, W. Sun, L. Fan, Y. Xie, J. Lin, Z. Lan, V. Stacchinii, A. Musiienko, Q. Hu, P. Gao, A. Abate, M.K. Nazeeruddin, Adv. Mater. 36 (2024) 2310800. https://doi.org/10.1002/adma.202310800.